



## Research Article

# Alternating current oxidation of Ti–6Al–4V alloy in oxalic acid for corrosion resistant surface finishing

Rafael Marinho Bandeira<sup>1</sup> · Galtiere Corrêa Rêgo<sup>2</sup> · Carlos Alberto Picone<sup>3</sup> · Julia van Drunen<sup>1,4</sup> · Wagner Rafael Correr<sup>2</sup> · Luiz Carlos Casteletti<sup>2</sup> · Sergio A. Spinola Machado<sup>1</sup> · Germano Tremiliosi-Filho<sup>1</sup>

Received: 6 January 2020 / Accepted: 13 May 2020 / Published online: 17 May 2020  
© Springer Nature Switzerland AG 2020

## Abstract

In this work, alternating current (AC) voltage ( $V_{AC}$ ) is applied to Ti–6Al–4V alloy in aqueous oxalic acid dihydrate solution to grow passive oxide films. The oxide layers are formed with  $V_{AC}$  values in the range of 10–80 V. The resulting surface oxide layers have estimated thicknesses in the 100–500 nm range and are expected to have a two-layer structure consisting of a porous outer layer and a compact inner layer. The AC anodization process is demonstrated to have a slight effect on the surface roughness. Porous regions are observed on the films formed at lower and high AC voltages (i.e.,  $V_{AC}$  10–30 and 80 V). The corrosion behavior in Ringer's solution over 48 h of exposure is studied with electrochemical impedance spectroscopy. The AC anodized samples have higher impedance values than the untreated alloy by more than an order of magnitude. The oxides formed at  $V_{AC} = 40 - 70$  V exhibit optimal resistance to corrosion as demonstrated by the overall impedance values, the polarization resistance values, and the capacitive behavior.

**Keywords** AC anodization · Ti–6Al–4V alloy · Oxide film · Corrosion

## 1 Introduction

Titanium alloys (Ti-alloys) are important in several technological applications [1]. They present hexagonal close packed (alpha phase) and body-centered cubic (beta phase) structures, which culminates in improved mechanical strength, formability and machinability [2, 3]. The excellent combination of mechanical resistance, low density, corrosion resistance (at relatively low temperatures), weldability, low instance of allergic reaction, and good biocompatibility make Titanium-based alloys excellent materials for applications in several areas such as aeronautical, automotive, marine, military, chemical, orthopedic, and dental [4–8]. The Ti–6Al–4V alloy belongs to the  $\alpha + \beta$  class and exhibits high strength, toughness, and excellent fatigue performance [9, 10]. Due to these and other advantageous

properties, Ti–6Al–4V is the most used alloy; it is used 60% more when compared to other Ti-alloys [1, 11]. Ti–6Al–4V stands out for its applicability as an orthopedic material when compared to stainless steel, cobalt alloys, and other metals, due to its low specific weight, biocompatibility, and better corrosion resistance [7, 12, 13]. Ti–6Al–4V, in general, has excellent corrosion resistance due to the formation of a superficial stable oxide film [14, 15]. However, in orthopedic applications, the corrosion behavior of Ti-alloys is not ideal because it can lead to the formation of rough, thick, and porous surface oxide films that contribute to chronic inflammation in the peri-implant tissues [16]. This happens because the human body provides an environment where problematic corrosion can occur due to the presence of proteins and oxygenated species [17, 18]. The wear/corrosion degradation of Ti-alloys can result

✉ Rafael Marinho Bandeira, rafael.marinho.bandeira@gmail.com | <sup>1</sup>Instituto de Química de São Carlos, Universidade de São Paulo, São Carlos, SP CEP 13566-590, Brazil. <sup>2</sup>Escola de Engenharia de São Carlos, Universidade de São Paulo, São Carlos, SP CEP 13566-590, Brazil. <sup>3</sup>Faculdade de Engenharia de Ilha Solteira, Universidade Estadual Paulista Júlio de Mesquita Filho, Ilha Solteira, SP CEP 15385-000, Brazil. <sup>4</sup>Metrohm Autolab B.V., Kanaalweg 29-G, 3526 KM Utrecht, The Netherlands.



in the release of debris and metal ions, cause hypersensitivity, cell damage, and tissue toxicity/carcinogenicity [19]. The metal ions released from Ti–6Al–4V can induce cytotoxicity due to elements like Al and V. Degradation of Ti–6Al–4V may occur due to interfacial contact with the corrosive biological environment, and mechanical wear (i.e. tribocorrosion) [20]. These factors limit the successful application of Ti-alloys and improvement is needed.

Anodization is a process used to thicken the native surface oxide on certain metals that are widely performed to improve the biological, chemical, and mechanical properties for engineering applications [12, 21, 22]. Titanium and Ti-alloys are often anodized with the aim of improving their biocompatibility and corrosion resistance. Traditional anodization involves passing direct current through the electrolytic cell with the subject of the process acting as the anode. Over the years, other processes using alternating current (AC) voltage have been applied to realize the same objective of creating a protective surface oxide. AC anodization of titanium and its alloys produces surface oxides layers with thicknesses that depends on the applied potential and duration of the anodization process [23–25]. Increase of the applied potential results in increasing oxide layer thickness [26]. The AC anodized implanted material is intended to be more biocompatible and corrosion-resistant due to the stable surface finishing. The goal is to reduce the need for surgical procedures to exchange failed or degraded implants [27–29]. One important strategy is to use protective coatings with low corrosion activity in the aggressive biological environment. Orthopedic and dental biomaterials must resist degradation in the presence of bacterial plaque, saliva, and other physiological fluids, movement of the body, etc., all of which can lead to material degradation.

Significant work exists to understand the corrosion behavior of Ti–6Al–4V alloys under simulated biological conditions by studying the corrosion in different electrolytes. Hsu et al. [20], studied the corrosion behavior of the Ti–6Al–4V alloy in urine, serum, and joint fluid (synovial fluid) using electrochemical techniques in a study that provides fundamental information on the biocorrosion of the untreated material (i.e. without coating or induced oxide formation).

In 1996, Jerkiewicz et al. [30] produced colored films on titanium electrodes and verified the formation of a passive oxide layer. They reported the formation of protective films by using  $\text{NH}_4\text{BF}_4$  solution as the electrolyte and applying AC voltages. The films presented a variety of colors that depend on the magnitude of the applied voltage. The color was attributed to an optical phenomenon called iridescence and is directly related to the thickness of the oxide layer. The relationship between the passive layer color and the thickness has been demonstrated for both

titanium and zirconium [30–32]. Uniform and homogeneous oxide films were studied with the variation of parameters such as applied voltage, polarization time, pH, and electrolyte concentration [25, 33]. The authors also demonstrated that the color of the passive films on titanium can be switched reversibly by increasing or decreasing the AC voltage due to the simultaneous formation and dissolution of the oxide during the anodization process [31]. This makes the oxide formation process even more tunable and easy to control.

In this work, we propose a new strategy to grow the surface oxide on Ti–6Al–4V by applying AC voltages in the presence of aqueous oxalic acid dihydrate solution to provide a suitable surface for use in biomedical applications. Our method is different than that of Jerkiewicz et al. [31] in the choice of electrolyte solution: oxalic acid solution is used instead of aqueous  $\text{NH}_4\text{BF}_4$ . Oxalic acid ( $\text{C}_2\text{H}_2\text{O}_4$ ) is a relatively strong organic acid commonly used in organic chemistry as a reducing agent [34]. It is considered harmful if swallowed or in direct contact with skin as it may cause skin burns and eye damage [35]. However, the toxicity is not of great concern since oxalic acid is poorly absorbed with a bioavailability of 2–5% [36]. Therefore, a subsequent study may be conducted to investigate the overall safety of aluminum alloys subjected to AC anodization in oxalic acid solution. Oxalic acid electrolyte is proposed to avoid the issue of fluoride toxicity for the tissue that is in contact with the surface of the treated metal. Surface analysis of AC anodized titanium with ammonium tetrafluoroborate ( $\text{NH}_4\text{BF}_4$ ) revealed that the oxide film contained Fluorine in the atomic percentage of 4–5% for the outer layer of the oxide film and 12–17% for the inner oxide layer [30]. Inorganic fluorides are generally highly corrosive and toxic; the effects resulting from exposure to fluorine compounds are due to the formation of hydrogen fluoride [37]. Therefore, we propose that AC anodization of the Ti–6Al–4V alloy in oxalic acid is a less dangerous procedure to obtain biocompatible surfaces.

## 2 Experimental

### 2.1 Preparation of the Ti–6Al–4V alloy

The composition of the commercial Ti–6Al–4V titanium alloy (Titanews Indústria e Comércio de Titânio LTDA, Brazil) used in this work is listed in Table 1. All samples were machined into a disk-shape with a diameter of 12 mm and 4 mm of thickness. The surfaces of the samples were sanded by using SiC papers with different grades (from 120 up to 2000 grit), followed by polishing with several colloidal silica solutions (size of 9, 5, 1, 0.3, and 0.05  $\mu\text{m}$ , in this order) with 10 wt% hydrogen peroxide. The polishing

**Table 1** The chemical composition of the Ti–6Al–4V alloy in weight percent

| Ti      | Al  | V   | Fe  | C    | N    | H     |
|---------|-----|-----|-----|------|------|-------|
| Balance | 6.1 | 3.9 | 0.2 | 0.01 | 0.02 | 0.012 |

process was performed to get a smooth surface with low roughness and is comparable to the preparations carried out in similar studies [20, 38]. The samples were then cleaned using an ultrasonic bath for 10 min in the following solvents: acetone, 2-Propanol, and deionized water (in order) followed by drying with hot filtered air.

## 2.2 Formation of the surface oxide films on Ti–6Al–4V via AC anodization

The oxide films were produced in a 10 wt% aqueous solution of oxalic acid dihydrate (Merck KGaA,  $\geq 99\%$ ) through the application of alternating current (AC) voltages ( $V_{AC}$ ) for 10 s at  $T = 298 \pm 2$  K in the voltage range of  $V_{AC} = 10 - 80$  V ( $V_{AC} = 10, 20, 30, 40, 50, 60, 70, \text{ or } 80$  V). A variable AC power source (JNG® Variac equipment model TDGC2-3) was used to apply the AC voltage and the AC potential was monitored by using a multimeter. During the oxide formation process, the Ti–6Al–4V alloy samples were placed in the solution at a distance of 10 cm from a second electrode, which was another disk-shaped Ti–6Al–4V electrode with the same size. The frequency of the AC voltages was 60 Hz in all cases. The AC anodized substrates were cleaned in an ultrasonic bath with deionized water for 10 min and dried with hot filtered air.

## 2.3 Optical and microscopic analysis of the electroformed oxide films

The optical images were acquired using a digital camera model Canon EOS Rebel T6. Scanning electron microscopy (SEM) coupled to energy-dispersive X-ray spectroscopy (SEM–EDS) was carried out with a Zeiss microscope model LEO 440, operating at 5 kV using a Si(Li) detector from Pentaflet. The images were acquired with the secondary electron detector at the pressure of 1 Pa. To obtain cross-section images of the AC anodized samples were cold embedded in epoxy resin and sanded laterally. The samples were polished with alumina up to 0.05  $\mu\text{m}$  and then etched with 5% hydrofluoric acid/30% nitric acid for 1 min. Then the samples were abundantly washed with deionized water and kept immersed in isopropyl alcohol until microscopic analysis was performed. The acid attack was done to remove the thin native oxide film that is formed after polishing the samples. The atomic force microscopy (AFM) was performed in a Nanosurf equipment model flexAFM and a controller

C3000 in contact mode, which investigated the presence of heterogeneities on the surfaces of the electrodes.

## 2.4 Electrochemical measurements

Electrochemical impedance spectroscopy (EIS) measurements of the electrodes were accomplished with a Metrohm Autolab potentiostat/galvanostat equipment (model PGSTAT30) equipped with a frequency response analyzer (FRA 2 module). The AC anodized samples were used as working electrodes. The reference electrode was a KCl saturated Ag/AgCl positioned close to the working electrode surface using a Luggin capillary. The counter electrode was a platinum sheet with a contact area of 4  $\text{cm}^2$ . The electrodes were exposed to Ringer's solution (purchased from *Baxter hospitalar LTDA*). Each 100 mL of Ringer's solution has the following contents: 800 mg of sodium chloride, 310 mg of sodium lactate, 30 mg of potassium chloride, and 20 mg of hydrated calcium chloride. Ringer's solution has a pH of approximately 6.5. The use of Ringer's solution as the test medium for the corrosion study is important because it simulates the human body fluid. EIS measurements were performed on all AC anodized electrodes to obtain information about the stability of the oxide films from 6 to 48 h of exposure in Ringer's solution. To compare the effect of the protection afforded by the passive oxide films, impedance measurements were also performed with the untreated Ti–6Al–4V alloy. The EIS measurements were acquired by applying a frequency range from  $10^5$  to  $10^{-1}$  Hz and an amplitude perturbation signal of  $\pm 10$  mV from the open circuit potential (OCP) value. The OCP was monitored for 6 h before the EIS measurement, a stable potential was reached and maintained throughout the EIS experiments. The EIS data was modeled by an equivalent electrical circuit model (using the ZView Software) based on the physical–chemical properties of the system. In this work, the applied equivalent circuit was similar to the suggested by Yazdi et al. [39] in which they used Ti–6Al–4V alloy to study the behavior of the oxygen diffusion on the modified alloy-surface. The equivalent circuit used to represent the impedance measurements of the untreated substrate (named 0 V) was the Randel's model.

### 3 Results and discussion

#### 3.1 Optical images of the electroformed oxide films

The oxide films were successfully formed on Ti-6Al-4V alloy with different applied AC voltages. Digital optical images of the electrodes were obtained with visible light as showed in Fig. 1. Therefore, the color of each electrode is the real color obtained for each  $V_{AC}$  value. Figure 1 shows that different colored surfaces were obtained as the applied voltage increased. The polished Ti-6Al-4V alloy displays a brilliant metallic finish. It is commonly accepted that light interference between the interfaces of the oxide film is responsible for the observed colors [40]. The coloration depends on the applied AC voltage value and originates from constructive light interference, due to the phenomenon that is known as iridescence [30, 32].

#### 3.2 SEM images and EDS analysis of the oxide films

SEM images of the passive oxide films formed on the Ti-6Al-4V alloy are displayed in Fig. 2. Figure 2a, c, and e show the surface of three oxide layers (formed with  $V_{AC} = 30, 50,$  and  $70$  V). These images show some inhomogeneity, including some dark and light regions. Figure 2b, d, and f show the surface of the same three passive layers at higher magnification for a better observation of the black and white features. Figure 2 b shows some scratches on the anodized electrode at  $V_{AC} = 30$  V which is a result of the sample pretreatment: polishing with SiC paper. The scratches are less prevalent for the layer formed at  $V_{AC} = 50$  V, and not observable for the layer formed at  $V_{AC} = 70$  V, Fig. 2d, f, respectively. The thickness of the oxide layer is expected to increase with

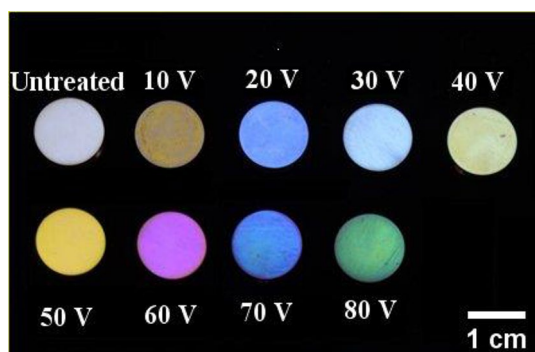


**Fig. 1** Oxide films produced on the Ti-6Al-4V alloy in the presence of oxalic acid through the application of several AC voltages between  $V_{AC} = 10 - 80$  V for 10 s at  $T = 298$  K. The untreated sample corresponds to the Ti-6Al-4V alloy without electrochemical treatment

increasing AC voltage and the thicker oxide layers have diminished the appearance of the scratches through modification of the surface. During the oxide formation process, there is a simultaneous dissolution of the surface material which has likely evened out the scratches [31]. The oxide films produced at  $V_{AC} = 30$  and  $70$  V exhibited micropores as indicated by arrows in Fig. 2b, f. No pores were observed in the sample anodized at  $V_{AC} = 50$  V, Fig. 2d.

Energy-dispersive X-ray spectroscopy analysis of the AC anodized surfaces was used to understand its composition. In Fig. 3 the EDS spectra are presented for the sample treated with  $V_{AC} = 50$  V. The regions analyzed are shown in Fig. 2d (points 1 and 2, indicated by arrows). The spectrum in Fig. 3a originates from point 1 (light region), the spectrum of Fig. 3b originates from point 2 (dark region). The dark regions, indicated by point 2, correspond to the presence of oxalic acid residue resulting from the film formation process. The black regions were dominant on the samples with passive films formed at  $V_{AC} = 30$  V compared with  $V_{AC} = 50$  V and  $V_{AC} = 70$  V. Light regions are attributed to the oxide film formed during the AC anodization process.

Table 2 summarizes the atomic percentage of the components acquired in two regions of the sample's surface. The dark regions observed in Fig. 2 are associated with oxalic acid residue and contain a detectable amount of carbon. The EDS spectrum for the light region shows that the oxide film is composed mainly of titanium oxide, but also contains a detectable amount of aluminum and vanadium.

Figure 4 presents SEM images of cross-sections for Ti-6Al-4V alloy subjected to AC anodization with  $V_{AC} = 10, 30,$  and  $60$  V. These cross-sections enable the observation of the material's microstructure from the surface to a depth of a few hundred micrometers. Based on the literature [30], the AC anodization process is expected to form a surface oxide with thickness in the 100–500 nm range (depending on the applied AC potential). Therefore, this oxide layer cannot be observed on the scale of these images. For each of the samples, we observe a difference in the microstructure towards the top (treated) surface of the sample. There appears to be an additional thick layer within each of the samples, with the thickness increases with applied AC potential (i.e.  $\sim 30$   $\mu\text{m}$  for  $V_{AC} = 10$  V;  $\sim 80$   $\mu\text{m}$  for  $V_{AC} = 30$  V;  $\sim 250$   $\mu\text{m}$  for  $V_{AC} = 60$  V). This structure does not appear to be a normal metal grain boundary because of its linear alignment in parallel to the samples' surface. To gain greater insight, EDS mapping of oxygen was performed on this structure for the  $V_{AC} = 30$  V sample (see Fig. 4d) and it was demonstrated that this thick layer contains a higher concentration of oxygen, compared with the material at greater depth. We speculate that the AC anodization process allows for the migration of oxygen to the bulk of the



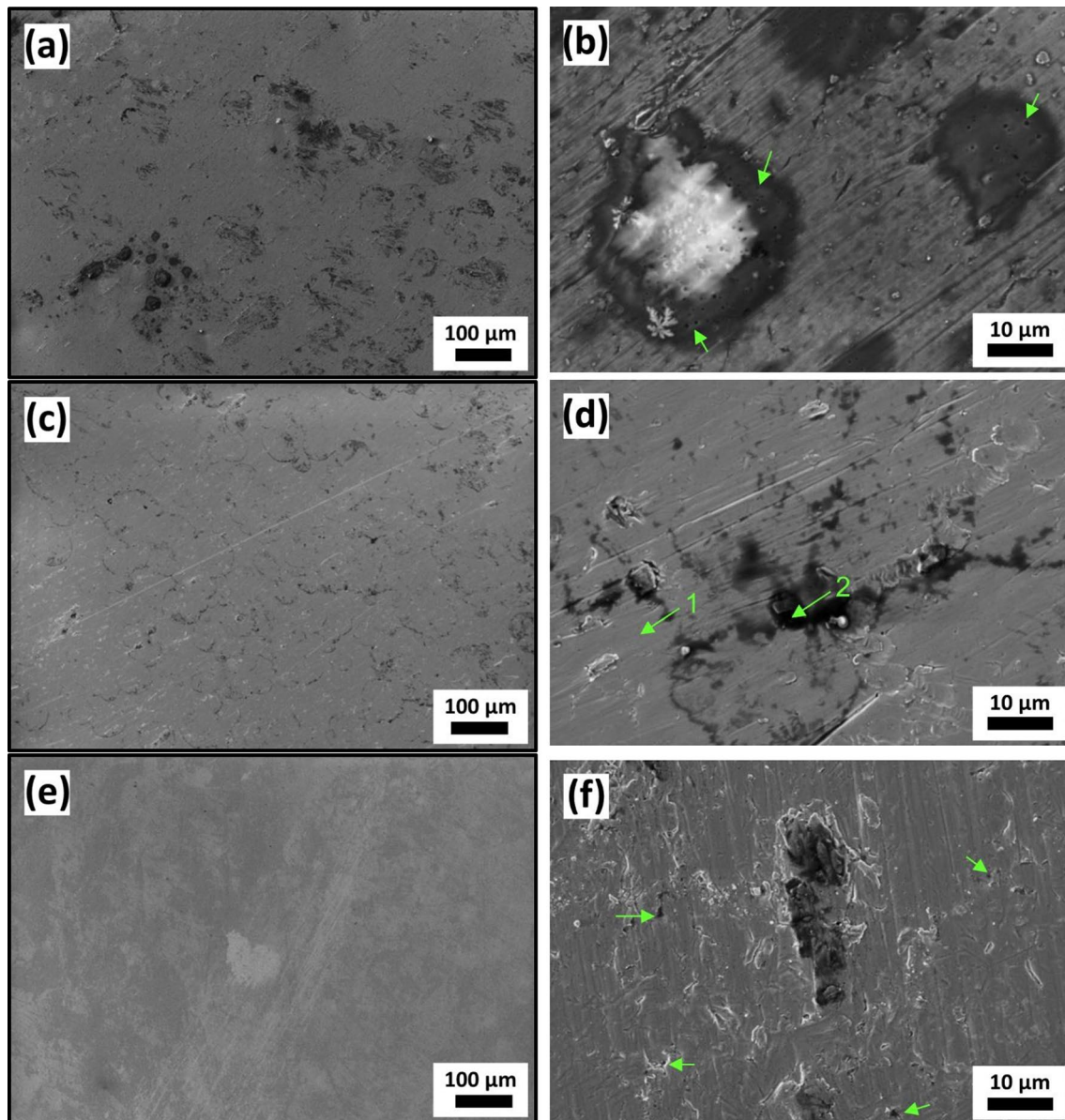


**Fig. 2** SEM images of the Ti-6Al-4V alloy surfaces after the application of AC voltages **a, b**  $V_{AC} = 30$  V, **c, d**  $V_{AC} = 50$  V, and **e, f**  $V_{AC} = 70$  V, each for 10 s at  $T = 298$  K

alloy. However, we do not have sufficient information to further qualify this structure.

### 3.3 The roughness of the electrodes

Atomic force microscopy images were acquired on some of the oxidized surfaces to analyze surface morphology and roughness. These properties are important because they influence the biocompatibility and corrosion behavior of the materials. The AFM images for samples treated with  $V_{AC} = 30, 50, 70,$  and  $80$  V are displayed in Fig. 5. These images reveal that the samples each have

different morphology. The average surface roughness ( $R_a$ ) values as determined by AFM are listed in Table 3. The surface of the sample treated with  $V_{AC} = 30$  V showed a  $R_a = 1.96 \pm 0.02$  nm, which is slightly higher than the untreated, polished Ti-6Al-4V alloy ( $R_a = 1.76 \pm 0.03$  nm). The surface formed at  $V_{AC} = 50$  V (Fig. 5b) presented a roughness value of  $R_a = 2.73 \pm 0.05$  nm but showed roughness maxima heights between 10 and 30 nm, in which there is a more homogenous surface appearance. Although the qualitative visual aspect of the surface obtained at  $V_{AC} = 50$  V presents fewer heterogeneities than  $V_{AC} = 30$  V, the presence of few points where the heights

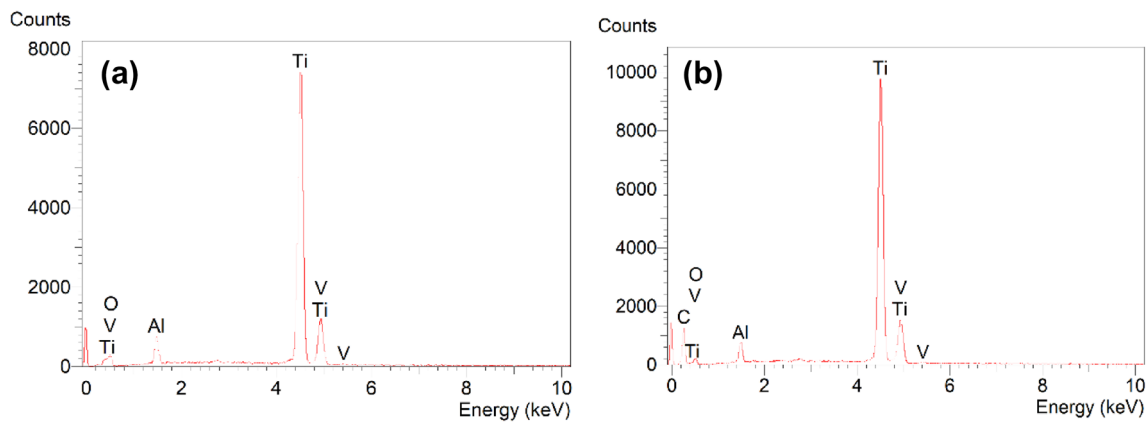


**Fig. 3** EDS spectra the sample treated with  $V_{AC} = 50$  V. The regions analyzed are shown in Fig. 2 d (points 1 and 2, indicated by arrows); **a** corresponds to the light regions (dominant regions) and **b** corresponds to the dark regions

**Table 2** Elemental composition of the anodized titanium alloy surface. The EDS correspond to the clear and dark regions indicated in Fig. 2d as point 1 and 2, respectively

| Element | Atomic (%) |         |
|---------|------------|---------|
|         | Point 1    | Point 2 |
| O       | 38.29      | 21.98   |
| Al      | 4.70       | 2.39    |
| Ti      | 54.88      | 35.23   |
| V       | 2.13       | 1.26    |
| C       | –          | 39.13   |

appear between 70 and 80 nm influences dramatically on the average surface roughness. The surface obtained with  $V_{AC} = 70$  V (Fig. 5c) displays numerous high points that were probably produced during the growth mechanism of the oxide film; the  $R_a$  value for this sample is  $3.4 \pm 0.06$  nm. In a similar study, small hemispherical particles were observed to be incorporated into oxide films formed with AC anodization on Ti using  $NH_4BF_4$  electrolyte. The authors

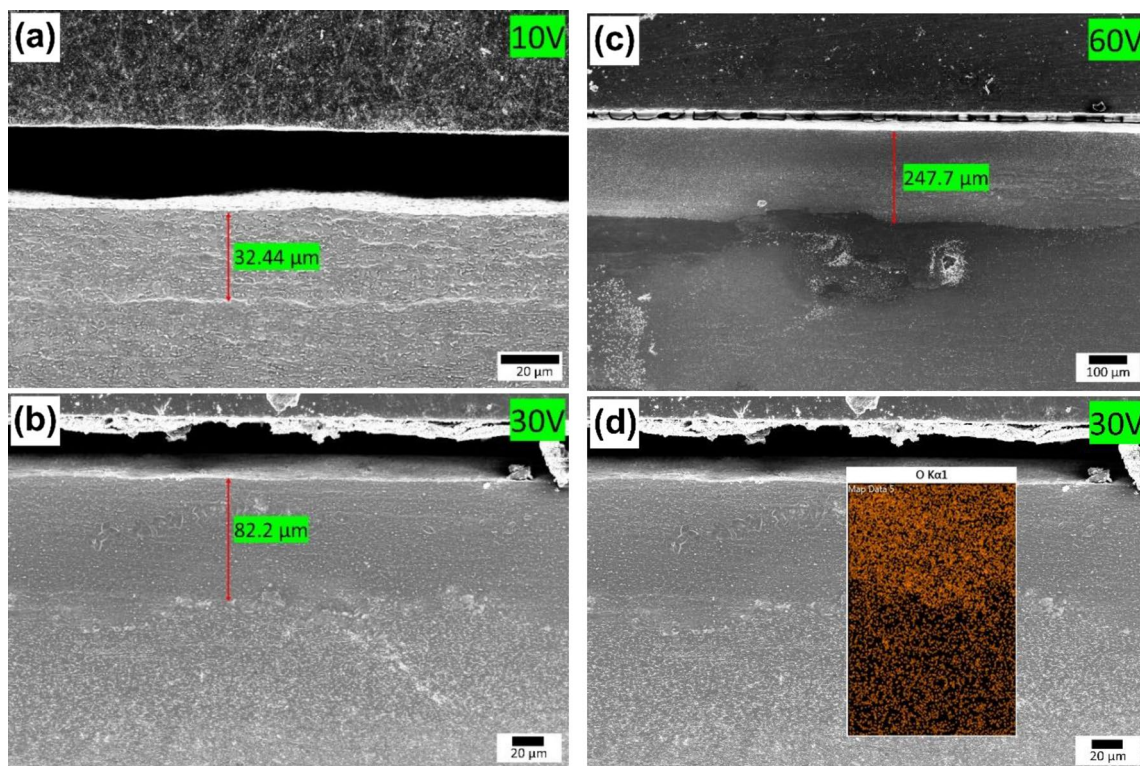


**Fig. 4** Cross-section images for the samples subjected to AC anodization with **a**  $V_{AC} = 10$  V, **b**  $V_{AC} = 30$  V, and **c**  $V_{AC} = 60$  V for 10 s at  $T = 298$  K. **d** SEM image of the electrode  $V_{AC} = 30$  V with a selected area for EDS elemental analysis mapping of oxygen



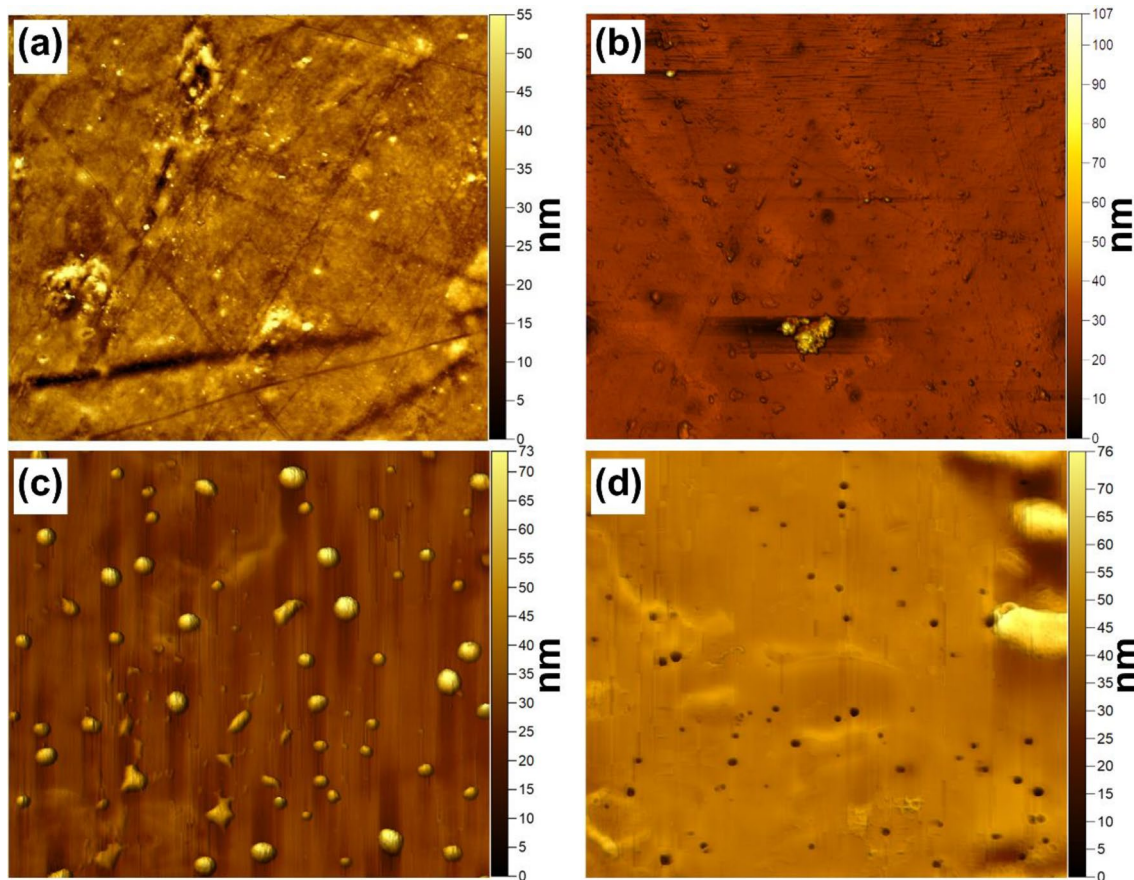


**Fig. 5** AFM images of samples subjected to the application of AC voltages **a**  $V_{AC}=30$  V, **b**  $V_{AC}=50$  V, **c**  $V_{AC}=70$  V, and  $V_{AC}=80$  V for 10 s at  $T=298$  K. For each image the area scanned was  $3\text{ mm}^2$

**Table 3** Average surface roughness ( $R_a$ ) of the untreated and anodized substrates

| Applied AC voltage | Average surface roughness, $R_a$ (nm) |
|--------------------|---------------------------------------|
| Untreated          | $1.76 \pm 0.03$                       |
| $30 V_{AC}$        | $1.96 \pm 0.02$                       |
| $50 V_{AC}$        | $2.73 \pm 0.05$                       |
| $70 V_{AC}$        | $3.4 \pm 0.06$                        |
| $80 V_{AC}$        | $4.84 \pm 0.08$                       |

concluded that these particles do not alter the structure of the protective surface oxide layer surrounding the particles [30]. Finally, the surface of the  $V_{AC}=80$  V sample electrode has  $R_a=4.84 \pm 0.08$  nm. These AFM measurements demonstrate that the surface roughness of the electrodes increases slightly with an increase in the magnitude of the AC applied voltages. Previous studies have demonstrated the  $R_a$  values are either not systematically affected by the AC anodization process [41], or that the  $R_a$  values decrease after AC anodization [32], and that there is no consistent

trend related to the magnitude of the applied  $V_{AC}$  [32, 41]. This is contrary to our findings. It is worth noting that these studies investigated rougher surfaces to begin with (Ti pretreated with micro-sandblasting and chemical etching) and that the measurements were done stylus profilometry, which is a less sensitive technique. The  $R_a$  values reported herein are on the order of a few nanometers which are within the experimental uncertainty of the profilometry measurements. Considering our AFM measurements and the profilometry measurement of previous studies, we conclude that the formation of the oxide films with the applied AC voltages is accomplished without drastic modification of the existing surface morphology. This is a desirable characteristic of this method, as the morphology of the surface may be first tuned using an appropriate pretreatment method before the AC anodization step. Rough surfaces have been proven to facilitate cell adhesion and osseointegration of an implant [42, 43], but may also give rise to increased metal ion release. The optimal surface roughness for a biocompatible material depends highly on the application and tunability of this parameter is important.

### 3.4 Electrochemical impedance spectroscopy results

The EIS measurements were acquired to evaluate the stability of the oxide films on Ti-6Al-4V alloy for 48 h of immersion in the corrosive Ringer’s solution. Bode modulus and Bode phase angle plots are presented in Figs. 6 and 7, respectively. In these plots, we show the impedance behavior of electroformed oxide films at exposure times of 6, 12, 24, and 48 h. In each plot, the result from untreated Ti-6Al-4V alloy is plotted for references and denoted 0 V in the legend.

The total impedance values of all electrodes prepared in this study were higher than similar types of protection described in related studies [38, 39, 44]. Table 4 summarizes the modulus of impedance acquired at low frequencies ( $10^{-2}$ – $10^{-1}$  Hz) for comparative studies in the literature. The comparison focuses on the low-frequency part of the EIS data because slow corrosion processes relating to charge and mass transfer at the oxide layers are probed at low frequency. Table 4 demonstrates that the films produced by AC anodizing using oxalic acid

show an increase in corrosion resistance by more than an order of magnitude when compared to other recent studies [38, 39, 44].

All electrodes offered very stable impedance values over the exposure period, which means that the oxide film has minimal anodic dissolution reaction. The electrodes obtained from the applied voltages between  $V_{AC} = 40 - 70$  V showed better stability than the electrodes obtained from higher or lower AC anodization voltages. The most stable surface was obtained at  $V_{AC} = 50$  V; this sample also showed superior polarization resistance at 48 h of exposure. The electrodes with protective passive oxides presented superior impedance values by more than an order of magnitude when compared to the untreated substrate (denoted 0 V). The Bode phase angle plots presented in Fig. 7 display curves in which samples produced between  $V_{AC} = 40$  and 70 V exhibit phase angle nearer to  $90^\circ$  at intermediate frequencies. This behavior indicates that these electrodes have superior capacitive behavior associated with the passive film when compared to the other electrodes. According to literature, the phase angles close to  $-90^\circ$

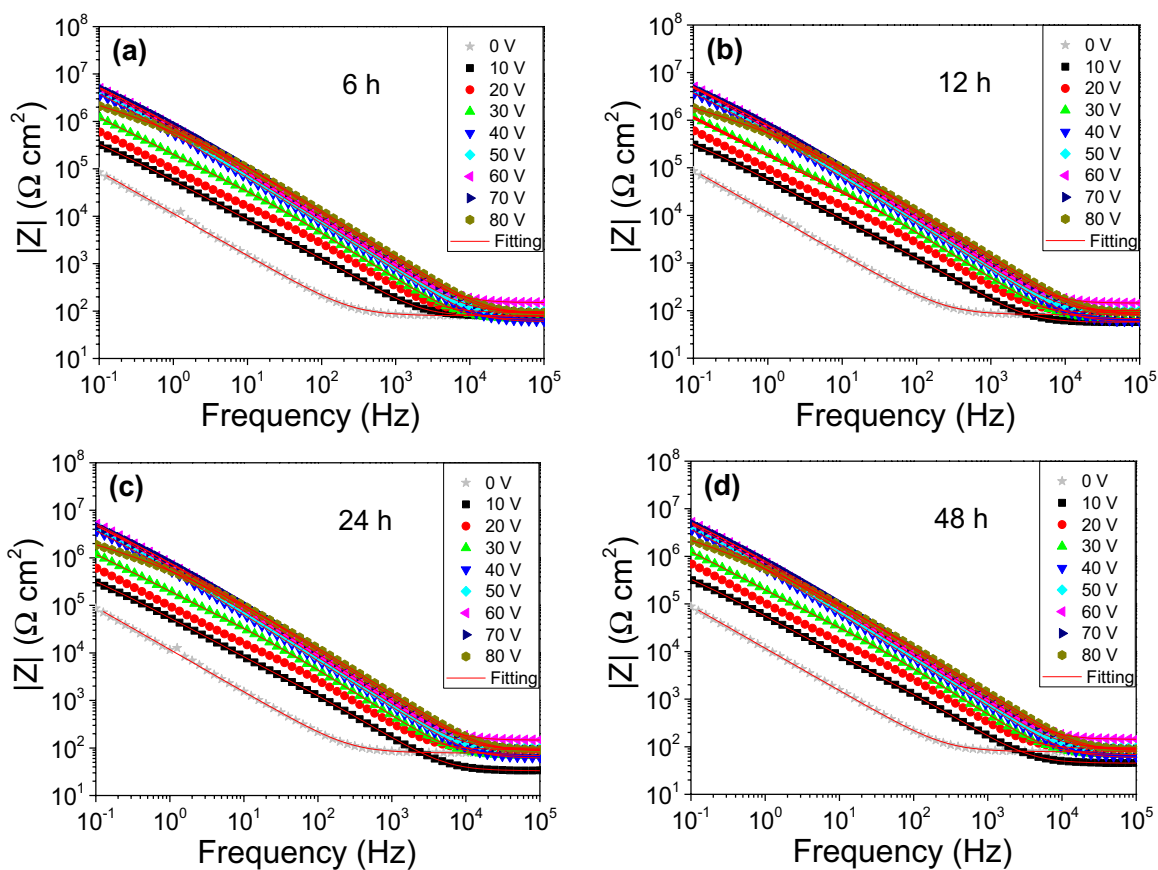


**Fig. 6** Bode modulus plots of the electrodes after 6, 12, 24 and 48 h of exposure in Ringer’s solution. The full red lines correspond to the applied fitting with the equivalent circuit shown in Fig. 8



**Fig. 7** Bode phase angle plots of the electrodes after 6, 12, 24 and 48 h of exposure in Ringer’s solution. The full red lines correspond to the applied fitting

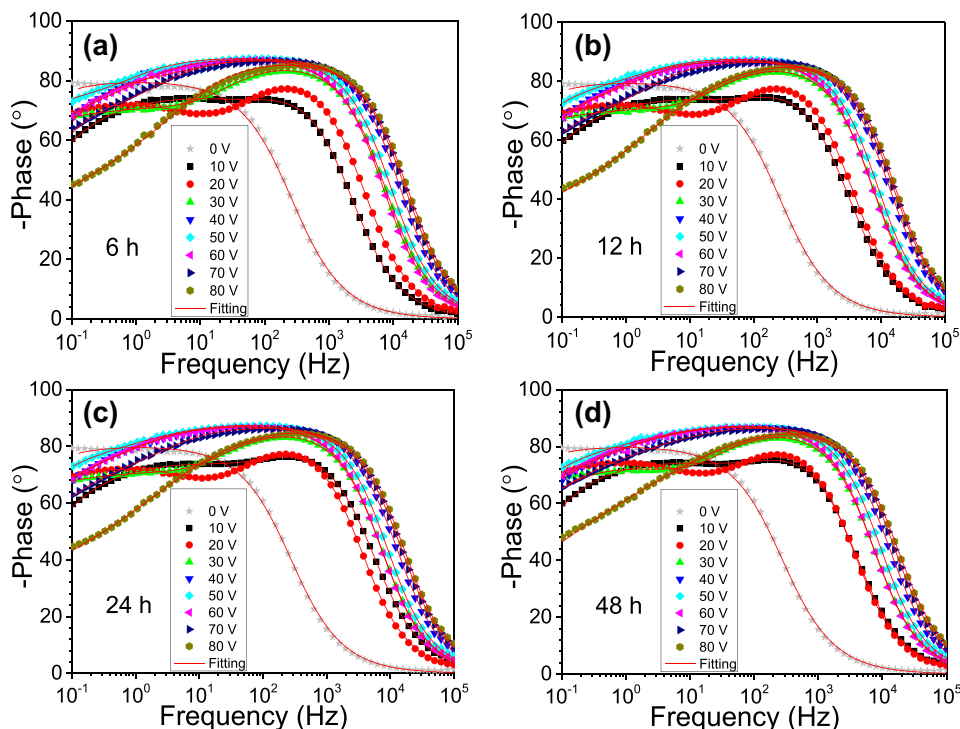


**Table 4** Comparison of impedance values ( $|Z|$ ) at low frequencies obtained in different studies and their corresponding corrosive medium

| Impedance ( $\Omega \text{ cm}^2$ ) at $10^{-2}$ – $10^{-1}$ Hz | Corrosive medium                   | References   |
|---|------------------------------------|--------------|
| $\sim 5.0 \times 10^5$  | Phosphate buffered saline solution | [38]         |
| $\sim 1.5 \times 10^5$  | Phosphate buffered saline solution | [39]         |
| $\sim 3.0 \times 10^5$  | Ringer’s solution                  | [44]         |
| $\sim 5.0 \times 10^6$  | Ringer’s solution                  | Current work |

are typical of a near capacitive behavior corresponding to the improved corrosion resistance of compact and uniform passive films [38, 45, 46].

The EIS data was fitted by an equivalent circuit [39] that was used to represent the components of a physical system. All fittings resulted in low  $\chi^2$  values (on the order of  $10^{-3}$  or lower) and errors were inferior to 4% for each fitted parameter. In the case of the untreated alloy, the equivalent circuit corresponds to the simplest Randel’s circuit (Fig. 8a) that includes a solution resistance ( $R_s$ ), a double-layer capacitor ( $CPE_1$ ) and a polarization resistance ( $R_p$ ). The untreated electrodes were used immediately after polishing and cleaning as described previously in the experimental section. Thus, the surface is covered with a thin native oxide that forms spontaneously on valve

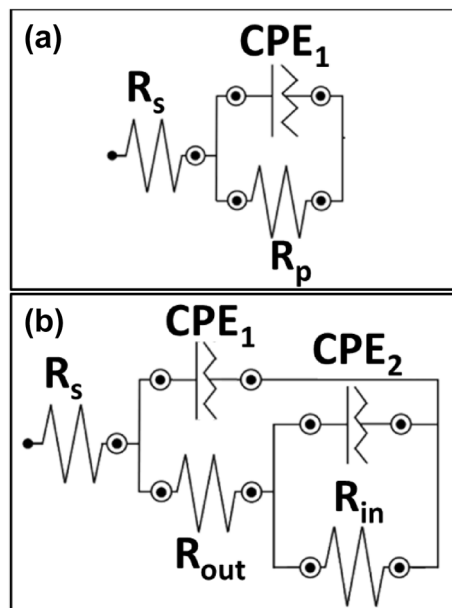


**Fig. 8** Equivalent circuit used to fit the EIS data for the **a** untreated and **b** anodized samples in oxalic acid solution

metals [47]. Our choice of this equivalent circuit is based on the observation that only one-time constant is evident in the EIS data for the untreated sample. Schneider et al. [48] offer a similar observation and interpretation in their study on pure titanium. For the AC anodized electrodes, the applied equivalent circuit (Fig. 8b) contains the following

elements: an  $R_s$  representing the solution resistance, a constant phase element (CPE<sub>1</sub>) representing the outer-passive layer of the oxide film, a constant phase element (CPE<sub>2</sub>) associated to the inner-passive layer of the oxide film, the resistance of the outer-passive oxide layer ( $R_{out}$ ), and the resistance of the inner-passive layer ( $R_{in}$ ). According to the literature [30, 39, 47, 49–51], the passive oxide films produced on Ti-based alloys are composed of two superimposed oxide layers. The first oxide layer, located on the top-surface (outer-passive layer) is porous and the

second oxide layer (inner-passive layer) exhibits a dense barrier-like structure.

Table 5 summarizes the fitted EIS data which indicates that the electrodes produced between  $V_{AC} = 40\text{--}70\text{ V}$  present the highest  $R_p$  values, which are the sum of the  $R_{out}$  and  $R_{in}$  resistances and correspond to the total corrosion resistance of the electrodes surface, Fig. 9c. In the case of untreated Ti–6Al–4V, the  $R_p$  value is associated with the total corrosion resistance of the polished alloy with its native oxide layer. The Bode modulus curves display

**Table 5** Impedance parameters obtained from fitted EIS data

| $V_{AC}$ (V) | Exposure time | $R_s$ ( $\Omega\text{ cm}^2$ ) | $CPE_{(1)}/Y_0$<br>( $s^n \times 10^{-7}$<br>$\Omega^{-1}\text{ cm}^{-2}$ ) | $n_1$ | $R_{out}$ ( $M\Omega\text{ cm}^2$ ) | $CPE_{(2)}/Y_0$<br>( $s^n \times 10^{-7}$<br>$\Omega^{-1}\text{ cm}^{-2}$ ) | $n_2$ | $R_{in}$ ( $M\Omega\text{ cm}^2$ ) | $R_p$ ( $M\Omega\text{ cm}^2$ ) | $\chi^2$           |
|--------------|---------------|--------------------------------|---|-------|-------------------------------------|---|-------|------------------------------------|---------------------------------|--------------------|
| 0            |               | 79.5                           | 169.3   | 0.89  | –                                   | –   | –     | –                                  | 1.46                            | $9 \times 10^{-4}$ |
| 10           | 6 h           | 78                             | 0.17  | 0.93  | $4.79 \times 10^{-3}$               | 0.23  | 0.70  | 1.5                                | 1.5                             | $3 \times 10^{-5}$ |
| 20           |               | 93                             | 7.75  | 0.95  | $1.58 \times 10^{-2}$               | 0.16  | 0.75  | 9.5                                | 9.6                             | $1 \times 10^{-5}$ |
| 30           |               | 67                             | 4.40  | 0.97  | $5.98 \times 10^{-2}$               | 7.91  | 0.68  | 77.3                               | 77.4                            | $1 \times 10^{-5}$ |
| 40           |               | 60                             | 2.72  | 0.97  | 1.64                                | 1.72  | 0.59  | 122.8                              | 124.4                           | $1 \times 10^{-4}$ |
| 50           |               | 96                             | 2.31  | 0.98  | 3.56                                | 1.21  | 0.67  | 131.0                              | 134.6                           | $1 \times 10^{-4}$ |
| 60           |               | 151                            | 1.92  | 0.98  | 2.39                                | 1.31  | 0.64  | 70.7                               | 73.1                            | $8 \times 10^{-5}$ |
| 70           |               | 86                             | 1.67  | 0.97  | 1.76                                | 1.32  | 0.72  | 20.8                               | 22.6                            | $1 \times 10^{-4}$ |
| 80           |               | 90                             | 1.54  | 0.97  | 0.29                                | 4.82  | 0.51  | 13.4                               | 13.7                            | $4 \times 10^{-4}$ |
| 0            |               | 81.5                           | 168.9   | 0.89  | –                                   | –   | –     | –                                  | 1.49                            | $4 \times 10^{-4}$ |
| 10           | 12 h          | 57                             | 0.18  | 0.93  | $4.86 \times 10^{-3}$               | 0.24  | 0.69  | 1.5                                | 1.5                             | $3 \times 10^{-5}$ |
| 20           |               | 91                             | 7.71  | 0.95  | $1.58 \times 10^{-2}$               | 0.16  | 0.75  | 10.0                               | 10.0                            | $1 \times 10^{-5}$ |
| 30           |               | 67                             | 3.91  | 0.97  | $5.45 \times 10^{-2}$               | 8.74  | 0.61  | 67.0                               | 67.0                            | $1 \times 10^{-5}$ |
| 40           |               | 57                             | 2.80  | 0.97  | 1.49                                | 1.75  | 0.65  | 81.5                               | 83.0                            | $9 \times 10^{-5}$ |
| 50           |               | 98                             | 2.27  | 0.98  | 2.11                                | 1.07  | 0.62  | 109.5                              | 111.6                           | $4 \times 10^{-5}$ |
| 60           |               | 143                            | 1.94  | 0.98  | 1.83                                | 1.22  | 0.61  | 52.8                               | 54.6                            | $4 \times 10^{-5}$ |
| 70           |               | 83                             | 1.73  | 0.97  | 1.55                                | 1.57  | 0.68  | 27.0                               | 28.5                            | $1 \times 10^{-4}$ |
| 80           |               | 88                             | 1.47  | 0.97  | $5.72 \times 10^{-2}$               | 5.54  | 0.44  | 17.7                               | 17.8                            | $8 \times 10^{-5}$ |
| 0            |               | 78.1                           | 164.4   | 0.89  | –                                   | –   | –     | –                                  | 1.52                            | $9 \times 10^{-4}$ |
| 10           | 24 h          | 33                             | 0.18  | 0.93  | $5.19 \times 10^{-3}$               | 0.24  | 0.70  | 1.4                                | 1.4                             | $3 \times 10^{-5}$ |
| 20           |               | 92                             | 7.68  | 0.95  | $1.53 \times 10^{-2}$               | 0.16  | 0.75  | 10.7                               | 10.7                            | $9 \times 10^{-6}$ |
| 30           |               | 69                             | 4.42  | 0.97  | $5.74 \times 10^{-2}$               | 8.03  | 0.68  | 65.8                               | 65.9                            | $9 \times 10^{-6}$ |
| 40           |               | 61                             | 2.78  | 0.97  | 1.39                                | 1.57  | 0.55  | 68.1                               | 69.5                            | $6 \times 10^{-5}$ |
| 50           |               | 98                             | 2.26  | 0.98  | 1.48                                | 1.02  | 0.60  | 98.0                               | 99.5                            | $3 \times 10^{-5}$ |
| 60           |               | 146                            | 1.96  | 0.97  | 2.07                                | 1.15  | 0.59  | 71.2                               | 73.3                            | $5 \times 10^{-5}$ |
| 70           |               | 87                             | 1.70  | 0.97  | 1.15                                | 1.58  | 0.63  | 32.7                               | 33.8                            | $8 \times 10^{-5}$ |
| 80           |               | 90                             | 1.44  | 0.97  | $8.26 \times 10^{-2}$               | 5.29  | 0.47  | 14.2                               | 14.3                            | $3 \times 10^{-5}$ |
| 0            |               | 78                             | 164.9   | 0.89  | –                                   | –   | –     | –                                  | 1.9                             | $2 \times 10^{-4}$ |
| 10           | 48 h          | 45                             | 0.18  | 0.94  | $4.78 \times 10^{-3}$               | 0.23  | 0.71  | 1.3                                | 1.3                             | $3 \times 10^{-5}$ |
| 20           |               | 91                             | 7.70  | 0.95  | $1.46 \times 10^{-2}$               | 0.13  | 0.77  | 9.7                                | 9.7                             | $1 \times 10^{-5}$ |
| 30           |               | 68                             | 4.49  | 0.97  | $5.43 \times 10^{-2}$               | 7.64  | 0.70  | 8.7                                | 8.8                             | $1 \times 10^{-5}$ |
| 40           |               | 59                             | 2.75  | 0.97  | 1.01                                | 1.65  | 0.56  | 93.4                               | 94.4                            | $7 \times 10^{-5}$ |
| 50           |               | 94                             | 2.03  | 0.99  | 1.02                                | 1.18  | 0.59  | 109.2                              | 110.2                           | $3 \times 10^{-5}$ |
| 60           |               | 143                            | 1.90  | 0.98  | 1.17                                | 1.12  | 0.60  | 77.6                               | 78.8                            | $7 \times 10^{-5}$ |
| 70           |               | 83                             | 1.67  | 0.97  | $6.78 \times 10^{-1}$               | 1.37  | 0.57  | 73.8                               | 74.5                            | $2 \times 10^{-5}$ |
| 80           |               | 85                             | 1.52  | 0.97  | $9.99 \times 10^{-2}$               | 4.29  | 0.53  | 11.6                               | 11.7                            | $5 \times 10^{-5}$ |

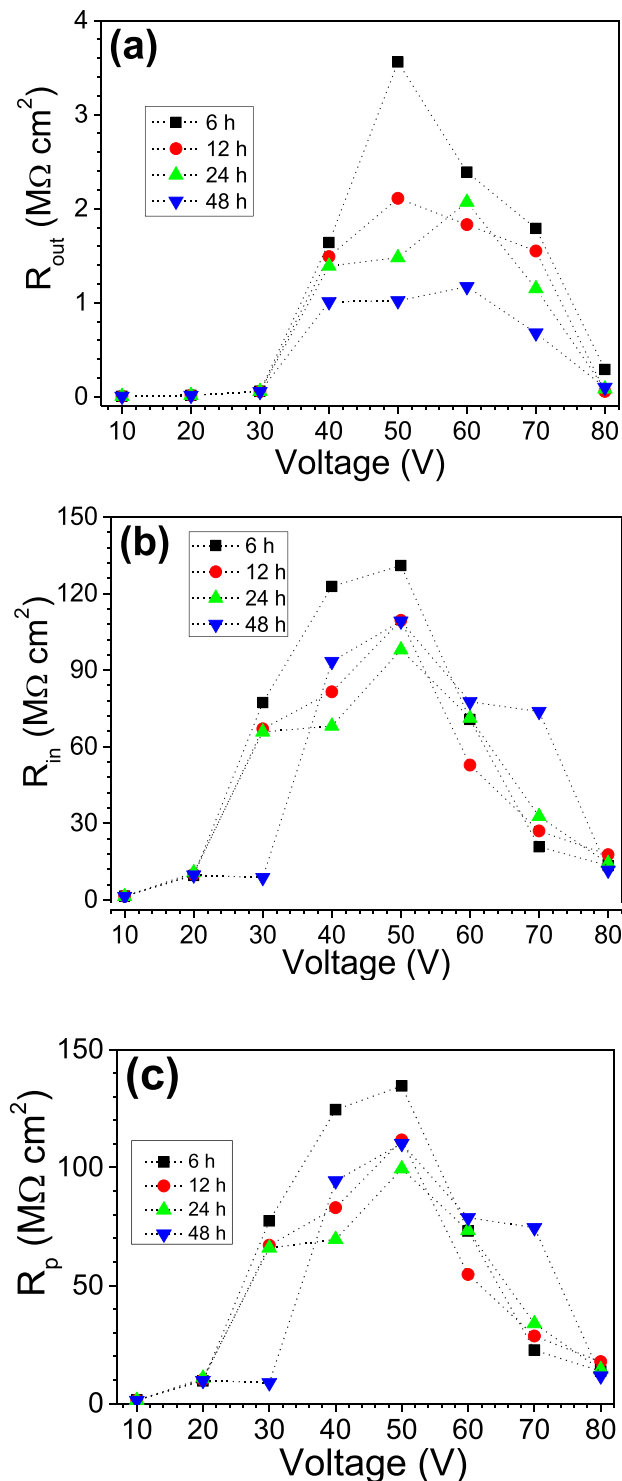


**Fig. 9** EIS data results acquired equivalent circuit modelling of the electrodes exposed to Ringer's solution up to 48 h: **a** Resistance of the outer-passive oxide layer ( $R_{out}$ ), **b** resistance of the inner-passive oxide layer ( $R_{in}$ ), and polarization resistance ( $R_p$ ). The values in the x-axis correspond to applied AC voltages used to form the surface oxides

similar behavior for all treated samples, which indicates that there are similar processes occurring. By looking at Table 5, there is a relatively low resistance of the outer-passive layer ( $R_{out}$ ) and higher resistance in the inner-passive layer ( $R_{in}$ ) of the passive film. The lower resistance of the outer-passive layer has been attributed to the presence of pores which saturate with Ringer's solution during prolonged exposure. The inner layer is characterized by the presence of a dense, compact oxide layer, as it has been reported in the literature [39, 49]. When looking at the  $R_{out}$  values, Fig. 9a, it was verified that the resistance of the outer-passive layer decreases with the exposure time. Therefore, the changes in the  $R_{out}$  values can be associated with solution uptake by the pores present in the outer layer of the oxide film.

The general trend of the  $R_{in}$  values is displayed in Fig. 9b. Note that the  $R_{in}$  is highest for the electrodes prepared at AC potentials of 40–70 V. This may be related to the fact that the films obtained at lower AC potentials (i.e. lower than 40 V) are thin and because the films obtained at the highest AC potentials (i.e. greater than 70 V) begin to develop defects such as the pores as observed in the AFM images. At applied AC voltages around 60 V<sub>AC</sub> and higher heating occurs near the edges of the sample and at the electrical contact, this introduces inhomogeneity and break down of the oxide in some regions [41]. The values of  $CPE_1$  are a little larger than  $CPE_2$ ; this is due to the first constant phase element being associated with a porous structure where the water uptake takes place, which culminates in increased capacitance values [52]. On the other hand, the decreased values of the  $CPE_2$ , with  $n_2$  between 0.5 and 0.8, is attributed to the thicker oxide layer. The Bode phase angle curves indicate that there are two time-constant domains which aligns with the proposed two-layer structure of the oxide. One of the time-constants appears with maximum phase angles between  $10^2$  and  $10^3$  Hz, and the second time-constant occurs with maximum phase angles between 0.1 and 1 Hz. The untreated samples exhibit just one time-constant as we can see from the phase angles curves, Fig. 7.

The AC anodization process has been applied to obtain stable, protective oxide layers on the surface of Ti and Ti-alloys. For an indication of the thickness of these layers, we largely rely on the literature. The relationship between applied AC voltage, oxide thickness, and the color of the resulting surface was studied in detail for Ti by the Jerkiewicz research group [25, 30–32, 41, 53, 54]. Based on the similarities of our method and the comparable colors obtained (see Fig. 1), we conclude that the oxide layers are in the 100–500 nm range, with increasing thickness as the AC applied voltage increases. It is possible to estimate the thickness of the layer from capacitance values derived from the EIS data, as described for untreated Ti in several



studies [47, 50]. Based on our equivalent circuit model, we may derive pseudocapacitance values from the  $CPE_2$  (inner layer) only, because it is in parallel with a resistor. Using the pseudocapacitance values for  $CPE_2$  the thickness of the inner oxide layers formed with  $V_{AC} = 30, 50, \text{ and } 70 \text{ V}$  are approximately 150, 250, and 360 nm, respectively. We caution that these values must be considered only as estimates with unknown experimental uncertainty as there are several concerns for the application of this method, including:

1. Determination of the thickness based on capacitance values loses some significance when pores are present [47];
2. The thickness calculation requires the dielectric constant of the material: we have used the standard value for  $TiO_2$  whereas the oxide material of this study incorporates Al and V; and
3. We cannot estimate the thickness of the outer oxide layer from the EIS data of this study.

We believe that the color of the obtained surface is a more valid indicator of the oxide thickness. We may compare our sample from  $V_{AC} = 30 \text{ V}$  (light blue, Fig. 1) with the “sky-blue” Ti oxide formed at  $V_{AC} = 26 \text{ V}$  in  $NH_4BF_4$  with the thickness of the oxide precisely measured to be  $295 \pm 9 \text{ nm}$  [30].

Although the thickness of the films is expected to increase linearly with an increase in the applied AC potentials, it is not possible to establish a direct relationship between the increase of thickness and the improvement of the corrosion protection. This is because the oxide films obtained from  $V_{AC} = 70 \text{ V}$  start to form defects that weaken their structure, decreasing the corrosion protection. Besides, the surface roughness for the samples obtained at  $V_{AC} = 70$  and  $80 \text{ V}$  are higher than the others, this also contributes to slightly poorer corrosion behavior.

## 4 Conclusions

Oxide films were successfully formed by AC anodization of Ti–6Al–4V alloy in an aqueous oxalic acid solution. The resulting materials exhibited various colors. The colors are indicative of the thickness of the oxide layers formed on the surface, and are comparable to the colors of similarly-treated Ti and Zr materials. The surface morphology and roughness are only slightly affected by the AC anodization technique presented herein. We conclude that this method can be applied to materials after an appropriate surface pretreatment is used to get the desired surface roughness and microstructure as AC anodization does not greatly alter the surface structure.

The stability of the materials towards corrosion in Ringer’s solution was evaluated with EIS during a 48-h exposure study. The EIS results align with the model where the oxide films have two distinct layers. The outer-layer being less resistant to corrosive attack due to the presence of pores, and the inner-layer being a dense and compact oxide. The presence of pores in the outer oxide layer was expected based on the literature, and was confirmed by SEM imaging. The EIS data corroborates this observation through the  $R_{out}$  values which decrease with increasing exposure time.

The thickness of the oxide films is expected to increase as the applied AC potential increases. Generally, a thicker barrier oxide provides greater corrosion protection. The results herein demonstrate that the oxide films produced by applying AC voltages between  $V_{AC} = 40 - 70 \text{ V}$  exhibit optimal resistance to corrosion as demonstrated by the overall impedance values, the polarization resistance values, and the capacitive behavior. These intermediate applied voltages produce films that are expected to be in the 100–500 nm thickness range and relatively free of defects introduced by localized heating and charge build-up during the AC anodization process.

All results described in this work indicate that the oxide films on Ti–6Al–4V demonstrate high resistance to corrosion in Ringer’s solution. The method used is simple, tunable, and reproducible. Therefore, AC anodization in the presence of oxalic acid should be a good option for the surface finishing of Ti–6Al–4V when intended for biomedical applications. To improve the fit towards this application, a reliable way to eliminate remnants of oxalic acid from the surface without causing damage to the protective film may be needed.

**Acknowledgements** This study was financed in part by the Coordenação de Aperfeiçoamento de Pessoal de Nível Superior—Brasil (CAPES)—Finance Code 001.

## Compliance with ethical standards

**Conflict of interest** The authors declare that they have no conflict of interest.

## References

1. Cui C, Hu B, Zhao L, Liu S (2011) Titanium alloy production technology, market prospects and industry development. *Mater Des* 32:1684. <https://doi.org/10.1016/j.matdes.2010.09.011>
2. Banerjee D, Williams JC (2013) Perspectives on titanium science and technology. *Acta Mater* 61:844. <https://doi.org/10.1016/j.actamat.2012.10.043>
3. Mohammed MT, Khan ZA, Geetha M, Siddiquee AN (2015) Microstructure, mechanical properties and electrochemical behavior of a novel biomedical titanium alloy subjected to

- thermo-mechanical processing including aging. *J Alloy Compd* 634:272. <https://doi.org/10.1016/j.jallcom.2015.02.095>
4. Romero A, García I, Arenas MA, López V, Vázquez A (2015) Ti6Al4V titanium alloy welded using concentrated solar energy. *J Mater Process Technol* 223:284. <https://doi.org/10.1016/j.jmatp.rotec.2015.04.015>
  5. Romankov S, Sha W, Ermakov E, Mamaeva A (2007) Characterization of interdiffusion growth of aluminized layer on Ti alloys. *J Alloy Compd* 429:143. <https://doi.org/10.1016/j.jallcom.2006.04.017>
  6. Sarraf M, Zalnezhad E, Bushroa AR, Hamouda AMS, Rafieerad AR, Nasiri-Tabrizi B (2015) Effect of microstructural evolution on wettability and tribological behavior of TiO<sub>2</sub> nanotubular arrays coated on Ti-6Al-4V. *Ceram Int* 41:7952. <https://doi.org/10.1016/j.ceramint.2015.02.136>
  7. Assis SL, Wolyneć S, Costa I (2006) Corrosion characterization of titanium alloys by electrochemical techniques. *Electrochim Acta* 51:1815. <https://doi.org/10.1016/j.electacta.2005.02.121>
  8. Sadeghi M, Kharaziha M, Salimijazi HR, Tabesh E (2019) Role of micro-dimple array geometry on the biological and tribological performance of Ti6Al4V for biomedical applications. *Surf Coat Technol* 362:282. <https://doi.org/10.1016/j.surfcoat.2019.01.113>
  9. Arrazola PJ, Garay A, Iriarte LM, Armendia M, Marya S, Le Maître F (2009) Machinability of titanium alloys (Ti6Al4V and Ti555.3). *J Mater Process Technol* 209:2223. <https://doi.org/10.1016/j.jmatp.rotec.2008.06.020>
  10. Sun W, Tan AWY, Khun NW, Marinescu I, Liu E (2017) Effect of substrate surface condition on fatigue behavior of cold sprayed Ti6Al4V coatings. *Surf Coat Technol* 320:452. <https://doi.org/10.1016/j.surfcoat.2016.11.093>
  11. Atar E, Kayali ES, Cimenoglu H (2008) Characteristics and wear performance of borided Ti6Al4V alloy. *Surf Coat Technol* 202:4583. <https://doi.org/10.1016/j.surfcoat.2008.03.011>
  12. Liu X, Chu PK, Ding C (2004) Surface modification of titanium, titanium alloys, and related materials for biomedical applications. *Mater Sci Eng R Rep* 47:49. <https://doi.org/10.1016/j.mser.2004.11.001>
  13. Ghoneim AA, Mogoda AS, Awad KA, Heakal FE (2012) Electrochemical studies of titanium and its Ti-6Al-4V alloy in phosphoric acid solutions. *Int J Electrochem Sci* 7:6539
  14. Milošev I, Metikoš-Huković M, Strehblow HH (2000) Passive film on orthopaedic TiAlV alloy formed in physiological solution investigated by X-ray photoelectron spectroscopy. *Biomaterials* 21:2103. [https://doi.org/10.1016/S0142-9612\(00\)00145-9](https://doi.org/10.1016/S0142-9612(00)00145-9)
  15. Pound BG (2014) Passive films on metallic biomaterials under simulated physiological conditions. *J Biomed Mater Res, Part A* 102:1595. <https://doi.org/10.1002/jbm.a.34798>
  16. Zhang Y, Addison O, Yu F, Troconis BCR, Scully JR, Davenport AJ (2018) Time-dependent enhanced corrosion of Ti6Al4V in the presence of H<sub>2</sub>O<sub>2</sub> and albumin. *Sci Rep* 8:3185. <https://doi.org/10.1038/s41598-018-21332-x>
  17. Addison O, Davenport AJ, Newport RJ et al (2012) Do 'passive' medical titanium surfaces deteriorate in service in the absence of wear? *J R Soc Interface* 9:3161. <https://doi.org/10.1098/rsif.2012.0438>
  18. Tengvall P, Lundström I (1992) Physico-chemical considerations of titanium as a biomaterial. *Clin Mater* 9:115. [https://doi.org/10.1016/0267-6605\(92\)90056-Y](https://doi.org/10.1016/0267-6605(92)90056-Y)
  19. Abdel-Hady Gepreel M, Niinomi M (2013) Biocompatibility of Ti-alloys for long-term implantation. *J Mech Behav Biomed Mater* 20:407. <https://doi.org/10.1016/j.jmbbm.2012.11.014>
  20. Hsu RW-W, Yang C-C, Huang C-A, Chen Y-S (2004) Electrochemical corrosion properties of Ti-6Al-4V implant alloy in the biological environment. *Mater Sci Eng, A* 380:100. <https://doi.org/10.1016/j.msea.2004.03.069>
  21. Li B, Shen Y, Luo L, Hu W, Zhang Z (2013) Surface aluminizing on Ti-6Al-4V alloy via a novel multi-pass friction-stir lap welding method: Preparation process, oxidation behavior and interlayer evolution. *Mater Des* 49:647. <https://doi.org/10.1016/j.matdes.2013.02.013>
  22. H-z Sun J, Zheng YS, Chi J, Y-d Fu (2019) Effect of the deformation on nitrocarburizing microstructure of the cold deformed Ti-6Al-4V alloy. *Surf Coat Technol* 362:234. <https://doi.org/10.1016/j.surfcoat.2019.01.079>
  23. İzmir M, Ercan B (2019) Anodization of titanium alloys for orthopedic applications. *Front Chem Sci Eng* 13:28. <https://doi.org/10.1007/s11705-018-1759-y>
  24. Wadhvani C, Brindis M, Kattadiyil MT, O'Brien R, Chung K-H (2018) Colorizing titanium-6aluminum-4vanadium alloy using electrochemical anodization: Developing a color chart. *J Prosthetic Dent* 119:26. <https://doi.org/10.1016/j.prodent.2017.02.010>
  25. Hrapovic S, Luan BL, D'Amours M, Vatankhah G, Jerkiewicz G (2001) Morphology, chemical composition, and electrochemical characteristics of colored titanium passive layers. *Langmuir* 17:3051. <https://doi.org/10.1021/la001694s>
  26. Cabrera N, Mott NF (1949) Theory of the oxidation of metals. *Rep Prog Phys* 12:163. <https://doi.org/10.1088/0034-4885/12/1/308>
  27. Narayanan R, Seshadri SK (2007) Phosphoric acid anodization of Ti-6Al-4V—Structural and corrosion aspects. *Corros Sci* 49:542. <https://doi.org/10.1016/j.corsci.2006.06.021>
  28. Xu H, Xing H, Dong A et al (2019) Investigation of gum metal coating on Ti6Al4V plate by direct laser deposition. *Surf Coat Technol* 363:161. <https://doi.org/10.1016/j.surfcoat.2019.01.086>
  29. Cho Y-S, Liao L-K, Hsu C-H et al (2019) Effect of substrate bias on biocompatibility of amorphous carbon coatings deposited on Ti6Al4V by PECVD. *Surf Coat Technol* 357:212. <https://doi.org/10.1016/j.surfcoat.2018.09.070>
  30. Jerkiewicz G, Strzelecki H, Wiekowski A (1996) A new procedure of formation of multicolor passive films on titanium: compositional depth profile analysis. *Langmuir* 12:1005. <https://doi.org/10.1021/la940578k>
  31. Jerkiewicz G, Zhao B, Hrapovic S, Luan BL (2008) Discovery of reversible switching of coloration of passive layers on titanium. *Chem Mater* 20:1877. <https://doi.org/10.1021/cm703052p>
  32. Holmberg RJ, Beauchemin D, Jerkiewicz G (2014) Characteristics of colored passive layers on titanium: morphology, optical properties, and corrosion resistance. *ACS Appl Mater Interfaces* 6:21576. <https://doi.org/10.1021/am506572m>
  33. Holmberg RJ, Bolduc S, Beauchemin D et al (2012) Characteristics of colored passive layers on zirconium: morphology, optical properties, and corrosion resistance. *ACS Appl Mater Interfaces* 4:6487. <https://doi.org/10.1021/am301389u>
  34. Fekry AM (2009) The influence of chloride and sulphate ions on the corrosion behavior of Ti and Ti-6Al-4V alloy in oxalic acid. *Electrochim Acta* 54:3480. <https://doi.org/10.1016/j.electacta.2008.12.060>
  35. Sigma-Aldrich (2019) Northwest Missouri State University, Maryville, USA. <https://www.nwmissouri.edu/naturalsciences/sds/o/Oxalic%20acid%20dihydrate.pdf>. Accessed 10 Dec 2019
  36. Dassanayake U, Gnanathanan CA (2012) Acute renal failure following oxalic acid poisoning: a case report. *J Occup Med Toxicol* 7:17. <https://doi.org/10.1186/1745-6673-7-17>
  37. NT Corporation (2019) Safety data sheet: ammonium fluoroborate. <https://noahotech.com/data/safety.17155.pdf>. Accessed 11 Dec 2019
  38. Bai Y, Gai X, Li S et al (2017) Improved corrosion behaviour of electron beam melted Ti-6Al-4V alloy in phosphate buffered saline. *Corros Sci* 123:289. <https://doi.org/10.1016/j.corsci.2017.05.003>

39. Yazdi R, Ghasemi HM, Wang C, Neville A (2017) Bio-corrosion behaviour of oxygen diffusion layer on Ti–6Al–4V during tribo-corrosion. *Corros Sci* 128:23. <https://doi.org/10.1016/j.corsci.2017.08.031>
40. Liu XM, Wu SL, Yeung KWK, Chung CY, Chu PK (2012) Surface Coloration and electrochemical impedance spectroscopy characterization of oxygen plasma implanted orthopaedic titanium alloys. *Int J Electrochem Sci* 7:6638
41. van Druenen J, Zhao B, Jerkiewicz G (2011) Corrosion behavior of surface-modified titanium in a simulated body fluid. *J Mater Sci* 46:5931. <https://doi.org/10.1007/s10853-011-5548-y>
42. Bowers KT, Keller JC, Randolph BA, Wick DG, Michaels CM (1992) Optimization of surface micromorphology for enhanced osteoblast responses in vitro. *Int J Oral Maxillofac Implants* 7:302
43. Boyan BD, Batzer R, Kieswetter K et al (1998) Titanium surface roughness alters responsiveness of MG63 osteoblast-like cells to  $1\alpha,25\text{-(OH)}_2\text{D}_3$ . *J Biomed Mater Res* 39:77. [https://doi.org/10.1002/\(SICI\)1097-4636\(199801\)39:1%3c77:AID-JBM10%3e3.0.CO;2-L](https://doi.org/10.1002/(SICI)1097-4636(199801)39:1%3c77:AID-JBM10%3e3.0.CO;2-L)
44. Bose S, Pathak LC, Singh R (2018) Response of boride coating on the Ti–6Al–4V alloy to corrosion and fretting corrosion behavior in Ringer’s solution for bio-implant application. *Appl Surf Sci* 433:1158. <https://doi.org/10.1016/j.apsusc.2017.09.223>
45. Tamilselvi S, Raman V, Rajendran N (2006) Corrosion behaviour of Ti–6Al–7Nb and Ti–6Al–4V ELI alloys in the simulated body fluid solution by electrochemical impedance spectroscopy. *Electrochim Acta* 52:839. <https://doi.org/10.1016/j.electacta.2006.06.018>
46. Alves VA, Reis RQ, Santos ICB et al (2009) In situ impedance spectroscopy study of the electrochemical corrosion of Ti and Ti–6Al–4V in simulated body fluid at 25 °C and 37 °C. *Corros Sci* 51:2473. <https://doi.org/10.1016/j.corsci.2009.06.035>
47. Pan J, Thierry D, Leygraf C (1996) Electrochemical impedance spectroscopy study of the passive oxide film on titanium for implant application. *Electrochim Acta* 41:1143. [https://doi.org/10.1016/0013-4686\(95\)00465-3](https://doi.org/10.1016/0013-4686(95)00465-3)
48. Schneider M, Schroth S, Schilm J, Michaelis A (2009) Micro-EIS of anodic thin oxide films on titanium for capacitor applications. *Electrochim Acta* 54:2663. <https://doi.org/10.1016/j.electacta.2008.11.003>
49. Alves AC, Wenger F, Ponthiaux P et al (2017) Corrosion mechanisms in titanium oxide-based films produced by anodic treatment. *Electrochim Acta* 234:16. <https://doi.org/10.1016/j.electacta.2017.03.011>
50. Assis SL, Costa I (2007) Electrochemical evaluation of Ti–13Nb–13Zr, Ti–6Al–4V and Ti–6Al–7Nb alloys for biomedical application by long-term immersion tests. *Mater Corros* 58:329. <https://doi.org/10.1002/maco.200604027>
51. Robin A, Carvalho OAS, Schneider SG, Schneider S (2008) Corrosion behavior of Ti–xNb–13Zr alloys in ringer’s solution. *Mater Corros* 59:929. <https://doi.org/10.1002/maco.200805014>
52. Bandeira RM, van Druenen J, Garcia AC, Tremiliosi-Filho G (2017) Influence of the thickness and roughness of polyaniline coatings on corrosion protection of AA7075 aluminum alloy. *Electrochim Acta* 240:215. <https://doi.org/10.1016/j.electacta.2017.04.083>
53. Munro A, Cunningham MF, Jerkiewicz G (2011) Spectral and physical properties of electrochemically formed colored layers on titanium covered with clearcoats. *ACS Appl Mater Interfaces* 3:1195. <https://doi.org/10.1021/am2000196>
54. Zhao B, Jerkiewicz G (2006) Electrochemically formed passive layers on titanium — Preparation and biocompatibility assessment in Hank’s balanced salt solution. *Can J Chem* 84:1132. <https://doi.org/10.1139/v06-142>

**Publisher’s Note** Springer Nature remains neutral with regard to jurisdictional claims in published maps and institutional affiliations.